Title

Performance Enhancement in Plasmonic Photoconductive Terahertz Electronics by Incorporating Distributed Bragg Reflectors

Author

Hemmati, Soroosh

Publication Date

2015

Peer reviewed|Thesis/dissertation

UNIVERSITY OF CALIFORNIA
Los Angeles

Performance Enhancement in Plasmonic Photoconductive Terahertz Electronics by Incorporating Distributed Bragg Reflectors

A thesis submitted in partial satisfaction
of the degree Masters of Science
in Electrical Engineering

by

Soroosh Hemmati

2015

ABSTRACT OF THE THESIS

Performance Enhancement in Plasmonic Photoconductive Terahertz Electronics by Incorporating Distributed Bragg Reflectors

by

Soroosh Hemmati

Master of Science in Electrical Engineering
University of California, Los Angeles, 2015
Professor Mona Jarrahi, Chair

Terahertz optoelectronics have shown significant promise in the development and enhancement of technologies in chemical identification, biological sensing, and medical imaging. The practical advancement of such devices, however, has been hindered by the characteristics of the frequency range, 0.3 to 3 THz in the electromagnetic radiation spectrum. Presented here is a demonstration of the significant advancements possible in creating efficient and ultra-fast plasmonic THz sources by incorporating an optical cavity using a distributed Bragg reflector (DBR). Plasmonic electrodes enable increased transmission of photons into a GaAs photo-absorbing substrate, and the DBR enhances the quantum efficiency of the device by creating an optical cavity which allows for nearly 100% of the incoming light getting absorbed in the active GaAs layer.

The thesis of Soroosh Hemmati is approved.

Benjamin Williams

Chee-Wei Wong

Mona Jarrahi, Committee Chair

University of California, Los Angeles

2015

To my parents, Zohreh Nejadian and Khalilallah Hemmati, and my wonderful sister, Soha, I dedicate this thesis. Your support at every step of the way was what got me through this degree. May this thesis be a constant reminder of my utmost love and respect for you!

Contents

List of Figures

List of Tables

Acknowledgments

I am truly grateful to my adviser, Prof. Jarrahi, for her continual guidance and support at every step of this research project. Had it not been for the insightful and timely help and guidance she provided me, this thesis in its current form would not have been possible. It was truly an honor working under a scientist as driven, diligent, focused and hardworking as Prof. Jarrahi. The lessons I learned from Prof. Jarrahi are ones I will cherish throughout my scientific career.

I am sincerely grateful to my committee, Prof. Benjamin Williams and Prof. Chee-Wei Wong, whose insightful comments and directive questions truly enhanced the quality of the work presented.

I would like to thank my dearest colleagues, Dr. Semih Cakmakyapan, Shang-Hua Yang, Nezih Tolga Yardimci, and Sabareesh Nikhil Chinta for their priceless collaboration on this project and the insight they provided at the most crucial steps of this research project.

Last but not least, I shall thank Prof. Mark Goorsky and Chao Li from the material science department for their assistance in generating the XRD results and determining the best simulation match between the simulations and XRD results. The author is also grateful to Baolai Liang and Mukul Debnath from the Intergrated Nano-Materials Laboratory (INML) at UCLA for their valuable input and also growing the wafers.

Chapter 1

Introduction

1.1 Current Technologies

The field of Terahertz electronics has seen rapid progress and innovation throughout the past three decades. The main goal in this field has been to produce compact, efficient and reliable sources (and detectors) capable of generating high power (detecting low power levels), and capable of working at temperatures close to the room temperature. This goal has been explored and approached through a number of different ways.

A fair amount of research has been put into extending the high frequency limit of radio frequency sources [1]. Among the techniques used in this area, resonance tunneling diodes, frequency multiplier chains, and Gunn diodes have been used to produce compact and promising sources [2-4]. The design and operation of these devices is rapidly improving, with multipliers reaching more than 1 mW output power in the 840-900 GHz frequency regime at room temperature [5], setting a stepping stone to enable sources in the 2-3 THz range with power levels high enough for multi-pixel imaging [6]. In addition, electron beam

devices such as travelling wave tube regenerative amplifiers and backward wave oscillators have shown reasonable power levels, even though pushing the output frequency of these devices above 1.5 THz has proven to be a challenge [7-9]. Backward wave oscillators also have the disadvantage of being bulky and requiring vacuum and high magnetic fields to operate.

Concurrently, a great deal of research has been put into pushing the low-frequency limit of optical emitters. Among such devices, quantum cascade lasers have shown great promise, and significant effort has been invested in pushing their output frequency lower and lower into the THz regime. Recently, output frequencies as low as 1 THz have been demonstrated and lower frequencies continue to be reached in this area [10]. The applicability of such devices has been limited, however, due to their bulky nature and requirement for a low operating temperature.

Other optical down-conversion technologies have also been investigated which are capable of producing high output power levels. These technologies have been in a large part based on nonlinear optical effects of a select few materials. The main challenge in the production of such devices, however, has been the optical-terahertz phase mismatch along the interaction path. Despite the usage of techniques such as quasi-phase matching in periodically poled media [11,12] and the use of tilted wave-front pump waves [13], the interaction path length is limited to a few centimeters, which also limits the output power levels, requiring high-power optical laser input power levels [14]. Despite these constraints, a GaSe-based source capable of producing continuously tunable and coherent radiation across the 0.18-5.27 THz range was demonstrated, with a peak output power of 69.4 W at 1.53 THz, corresponding to a photon conversion efficiency of 3.3% [15].

1.2 Photoconductive Terahertz Sources

Photoconductive optical-to-terahertz power generation has shown great promise and continues to be the most useful technique in terahertz-generation since it was first demonstrated [14, 16-23]. A main difference between optical-down-conversion and optical-to-terahertz techniques, as will be explained in the following section, is the former's inherent limit due to the law of conservation of photons, i.e. the Manley-Rowe limit. Where for every incident photon there is at most one emitted THz photon in the optical down-conversion techniques, optical-to-terahertz generation is not bound by this limit since every electron-hole pair produced can lead to the generation of multiple terahertz photons emitted from a suitable antenna. As a result, it is possible to, theoretically, reach 100% optical-to-terahertz efficiency. Despite such theoretical advantage, electron screening effect and low absorption of photo-produced electron-hole pairs have hindered the operation of these devices. In the following section we describe the techniques used to overcome these challenges.

Principles of operation

Photoconductive THZ emitters operate based on an incident optical pump producing electron-hole pairs in a photo-absorbing semiconductor. With a suitable voltage applied between the anode and the cathode, these generated charges will then drift toward their corresponding contact electrodes. If the photocurrent is produced from a sub-pico-second optical pulse or by heterodyning two continuous-wave (CW) optical beams with a THz frequency difference, the generated pulsed or CW THz current will lead to THz wave radi-

ation, assuming the current is fed into an antenna designed to radiate in the THz regime [24]. For optimal efficiency of radiation, it is desirable for the carriers to reach their corresponding contact electrodes within a fraction of the oscillation period of the desired radiation [25]. As a result, using short-carrier lifetime, high mobility substrates is beneficial since it allows for the ultra-fast carrier transport required for THz emission.

Photoconductive emission has become very promising considering the recent advances in solid-state electronics and fiber lasers [24]. There currently exist lasers capable of producing more than 10 W of power, narrow line-width in the KHz range, and wavelength tunability in the order of tens of nm, with center wavelengths at 1550 nm and 1030 nm. As a result, there is a lot of room for development of cost-effective, compact, and efficient THz systems.

There exist, however, a few challenges that stand in the way of producing high-power and efficient THz sources. First, assuming a nominal carrier drift velocity of $\sim 10^7$ cm/s, only those generated within 100 nm of the electrodes are able to reach their corresponding contact electrodes in less than a pico-second. This means that the rest of the carriers generated, which in conventional designs account for most of the generated carriers, just add to the DC current flowing between the electrodes, reducing the acceleration of fast carriers. This reduces the efficiency and THz power generation of the device. As a result, most conventional photoconductive THz sources use short-carrier lifetime active regions to reduce the DC current by quickly absorbing the slow carriers back into the semi-conductor. Low-temperature (LT) grown GaAs active substrates have been used extensively, with optical pump wavelength centered around 800 nm, due to the short carrier lifetime of LT GaAs at room temperature. Diffraction limit is another limiting factor in the operation of photo-

conductive THz sources. With optical pump wavelengths being mostly in the $750 - 1550$ nm region, it is commonplace for the distance between electrodes to be at least ~ 2 μm [17]. Based on what we mentioned before, regarding the useful range of less than 100 nm, it is clear that a really large portion of the generated carriers will not lead to the emission of THz radiation. Additionally, using higher optical pump power levels leads to increased carrier screening effect and thermal breakdown, resulting in degradation in the operation of the device and reduced quantum efficiency. Quantum efficiency is an important parameter describing the operation of the device since it has a quadratic relation with the power generated, due to the quadratic relationship between the ultra-fast current and THz power level generated. These limitations greatly increase the importance of using novel techniques to overcome diffraction-limited operation, carrier screening at high powers, slow current, and low quantum efficiency.

A number of ideas have been explored to address the challenges mentioned. Using short-carrier lifetime substrates has been a really commonly used technique. Based on the optical wavelength of the device, the material to be used differs significantly. Low temperature (LT) grown GaAs and ErAs introduced GaAs, low temperature grown InGaAs, ion irradiation of InGaAs, and introducing ErAs islands while growing InGaAs, have been two commonly used sets of materials for operation at 800 nm, and 1030 nm or 1550 nm, respectively. Although all these materials have a higher number of trapping sites, and therefore, lower carrier life-time than their intrinsic form, their usage is associated with low mobility and reduced thermal conductivity which could lead to thermal breakdown of the active layer at high optical pump power levels [26]. As a result, more needs to be done to enhance the overall efficiency of these devices.

A particularly successful approach has been the incorporation of plasmonic contact electrodes into photo-conductive THz sources. Plasmonics is the study of the interaction between electromagnetic waves and free electrons of a metal. By using a suitable geometry for the electrodes on the top, it is possible to couple the incident optical pump radiation onto the free electrons in the electrodes and consequently, transfer this energy into the semiconductor leading to the generation of electron-hole pairs [14, 24-26]. Using plasmonic contact electrodes overcomes the diffraction limit problem since in many cases, plasmonic contact electrodes can be designed to cover large portions of the active area of the semiconductor [24, 26, 27]. In addition, using plasmonic contact electrodes substantially reduces the transport path length of the photo-generated electron-hole pairs since most of the coupled optical photons get absorbed very close to the surface of the electrodes. As a result, it is not necessary to use short-carrier life-time semiconductors for efficient operation. Therefore, through operating beyond the diffraction limit, it is possible to reach much higher optical-to-terahertz conversion efficiencies [24].

Current state-of-the-art

Here we take a look at the most recent power, efficiency, and frequency levels reached using photoconductive THz sources. In 2013, the performance enhancement of a plasmonically enhanced photoconductive source was compared against that of an equivalent conventional photoconductive source (with no plasmonic gratings), and it was shown that the THz source using plasmonic gratings could emit up to 50 times more power than its equivalent conventional counterpart in the $0.1 - 1.5$ THz frequency band [14]. Another pho-

toconductive source based on three-dimensional plasmonic contact electrodes was demonstrated in 2012, with a peak broadband (0.1-2 THz) output power level of 105 μW in response to a 1.4 mW optical pump, corresponding to a 7.5% optical power to THz power efficiency [27]. Moreover, record-high broadband THz radiation power levels, reaching 3.8 mW (total radiated power) across the $0.1 - 5$ THz range, were demonstrated based on a design incorporating plasmonic nano-antennas, illustrating an order of magnitude higher optical-to-terahertz conversion efficiency compared to an equivalent conventional design [28]. This thesis will demonstrate how the inclusion of a distributed Bragg reflector (DBR) will enhance the photo-current even further, and lead to higher power and optical-to-terahertz efficiencies.

1.3 Breakdown of This Thesis

This thesis describes the author's contribution to the advancement of operation of photoconductive terahertz sources by incorporating a distributed Bragg reflector, among other things, to increase the quantum efficiency of the device, which as previously mentioned, has a quadratic relation with the THz power generated [24]. As will be shown later, this novel idea helps increase the absorption of the optical light to more than 95%, as shown in figure 2.7. The requirements and theoretical challenges of the problem will be introduced first along with the possible solutions. Then, the most feasible hypothesis will be presented based on the existing practical challenges. Once the foundation for the work is laid, the design of the structure at hand will be explored completely, and simulation results will be illustrated. The implementation of the design and its evaluation will come next. Finally, the results gained from this thesis project so far will be presented.

Chapter 2

Design

2.1 Requirements and Specifications

Theoretical Necessities

The requirements for a conventional ultra-fast opto-electronic THz source are short carrier life-time and considerable absorption at the optical pump frequency. Due to the higher speed of electrons than holes, a lot of opto-electronic THz sources work asymmetrically, meaning only one electrode is illuminated by the optical source [24, 27, 28]. Although not necessary, this method has proved to enhance the efficiency of the device and increase the output power levels. For high output power, it is necessary to have a material with high enough absorption coefficient at the optical pump frequency. In addition, to increase the external quantum efficiency of the device, it is favorable to have as much optical power transmitted to the active layer from the air as possible. This implies that the geometry of the plasmonic electrodes on the top must be designed carefully to maximize transmis-

sion. In addition, as with any other opto-electronic THz source, carrier screening is a major problem which needs to be dealt with. Specifically, in asymmetric devices, it is vital to address electron-electron screening. This phenomenon again, would add restrictions to the size and geometry of the plasmonic structure on the top. Finally, the electric field near the plasmonic gratings needs to be high enough to have the electrons travel in the mobility saturation regime of the semi-conductor.

Other requirements include high active layer thermal conductivity and lattice matching between consecutive layers of the wafer. Thermal conductivity is vital for high-power electronics due to the amount of heat dissipated during operation.

Finally, a device incorporating a distributed Bragg mirror needs to maintain lattice matching throughout the layers of the device to ensure that the optical and more importantly, electrical properties of the active layer will not degrade. In addition, due to the probable difference between the band gap of the top DBR layer and GaAs, one needs to ensure the added properties of the heterojunction are not detrimental to the operation of the device.

Design Specifications

The optical pump we worked with was a tunable high-power Ti-Sapphire laser operating in the regime 700-840 nm. As a result, the device was set to operate at an optical pump wavelength of 780 nm. In addition, due to the availability of high quality GaAs wafers and their relatively low cost, GaAs was selected to be the active layer. This selection narrows down the types of materials feasible for the operation of the device. First, to have a lattice-matched device, it is necessary to choose materials that possess the same lattice

constant at room temperature ($\sim$ 300 k). Fortunately, all $Al_xGa_{1-x}As$ materials possess extremely close lattice constants at room temperature. In addition, the band-gap of $Al_xGa_{1-x}As$ follows the following equation [29]:

$$E_G = 1.424 + 1.247x \ \text{(ev)} \ \ x < 0.45$$

$$E_G = 1.9 + 0.125x + 0.143x^2 \ \text{(ev)} \ \ x > 0.45$$

Furthermore, the photon energy of 780 nm light is

$$E = hf = \frac{hc}{\lambda} = 1.591 \ \text{(ev)}$$

This implies that for any fraction, x, greater than 0.134, $Al_xGa_{1-x}As$ would not absorb any light.

A requirement in the design of a Bragg mirror is for the reflection coefficients of the consecutive layers to be as far away from each other as possible, since the reflectivity of a Bragg mirror is given as [30]:

$$R = \left[\frac{n_0(n_2)^{2N} - n_s(n_1)^{2N}}{n_0(n_2)^{2N} + n_s(n_1)^{2N}}\right]^2 = \left[\frac{n_0(\frac{n_2}{n_1})^{2N} - n_s}{n_0(\frac{n_2}{n_1})^{2N} + n_s}\right]^2$$

$$= \left[\frac{(\frac{n_2}{n_1})^{2N} - 1}{(\frac{n_2}{n_1})^{2N} + 1}\right]^2 \quad \text{when} \ \ n_0 = n_s \tag{2.1}$$

Where in our design n_0, n_1, n_2, n_s, denote the reflection coefficients of the active layer (SI-GaAs), first layer of the DBR, second layer of the DBR, and the substrate (SI-GaAs), respectively. In addition, it is clear that the higher the number of periods of a distributed Bragg mirror, the higher the reflection coefficient of the total DBR.

The bandwidth of a Bragg mirror is given as [30]:

$$\mathrm{BW} = \frac{\Delta f_0}{f_0} = \frac{4}{\pi} \sin^{-1}\left(\frac{n_2 - n_1}{n_2 + n_1}\right)$$

As a result, for materials whose reflection coefficient hovers around 3.5, (therefore, $n_1 + n_2 \approx 7$), maximizing the ratio of n_1 and n_2 is favorable. Since the data for the refractive index of all AlGaAs compositions is not available (at least to the author's best knowledge), we selected $Al_{0.32}Ga_{0.68}As$ and AlAs to be the compositions of our DBR layers, with $n(Al_{0.32}Ga_{0.68}As) = 3.43$ and $n(\mathrm{AlAs}) = 3.00$ [29]. Using equation (2.1), we expect the following reflectivity from the DBR (Assuming $n(\mathrm{GaAs}) = 3.6835$ [29]):

N	R
1	0.018
5	0.342
10	0.760
15	0.931
20	0.981
25	0.995

Table 2.1: DBR reflectivity as a function of N

Because of the expected values shown in table 2.1, we decided to design the structure with 25 periods.

The next step was to find an estimate for the thickness of each layer. It is expected for a DBR with only two different materials to have layer thicknesses close to a quarter wavelength. As a result, our initial guess for $Al_{0.32}Ga_{0.68}As$ and AlAs thicknesses were 57 nm and 65 nm, respectively.

Once the estimates for the DBR composition and thickness were decided, the design of the plasmonic structure on top of the active GaAs layer was to be found. Once again, the

main requirement for this step was maximizing the trapping of the optical input inside the structure. This implies maximizing transmission of the 780 nm light into the structure and minimizing the transmission of the 780 nm light from the structure into the air. Solving this problem involves optimizing for three parameters: the thickness of the top DBR layer, the thickness of the GaAs active layer, and the geometry of the plasmonic gratings.

The most important aspect of the optimization process mentioned above is picking the correct thickness for GaAs because it has the largest effect on the electrical properties of the device. A thick GaAs layer is not desired since carriers absorbed too far from the electrodes will either be recombined or reach the electrodes too late, both of which lead to low optical-to-terahertz efficiency. A thin GaAs layer, however, could lead to not enough carriers being generated or thermal breakdown at moderate optical pump power levels. Furthermore, the active layer should be thick enough to ensure that the heterojunction due to the interface between GaAs and the top DBR layer does not negatively affect the electron transport from GaAs to the electrodes. As a result, the thickness of the GaAs layer was selected to be at most 200 nm and the other parameters were optimized based on this number. The process of finding the optimum grating geometry and the top DBR layer thickness involved running parametric simulations on the device, both optically (using COMSOL Multiphysics and Lumerical), and electrically (using Sentaurus).

The last piece of the design to be optimized is an anti-reflection coating on top of the gratings to both increase transmission of the optical light into the device and avoid oxidation of the gratings and GaAs during operation, especially at high optical pump powers. The most accessible options we had for such material were Silicon Nitride and Silicon Dioxide. Silicon Nitride was selected due to its higher reflection coefficient at 780 nm which would

enhance the transmission of light into the device.

2.2 Design Procedure

The previous section established a few preliminary parameters and a roadmap toward completing the design. This section shows the steps involved and results achieved during the optimization process.

As previously mentioned, the initial values to be used for optimizing the DBR structure are 57 nm and 65 nm for $Al_{0.32}Ga_{0.68}As$ and AlAs, respectively. The thickness of the active GaAs layer is assumed to be less than 200 nm and the geometry of the gratings and the thickness of the top $Al_{0.32}Ga_{0.68}As$, GaAs, and Si_3N_4 layers are yet to be determined based on simulation results.

Optimizing the Cavity Design

Table 2.2 summarizes the percentage of optical light absorbed by the active layer and electrodes as the grating geometry is gradually changed. For the data shown in table 2.2, the thickness of the GaAs and top $Al_{0.32}Ga_{0.68}As$ layers are 200 nm and 270 nm, respectively. In addition, a 370 nm Silicon Nitride anti-reflection coating is included. The distance between each pair of consecutive grating electrodes is fixed at 100 nm.

The data in table (2.2) illustrate the kind of approach done to optimize the design. As one can observe from the table, the lower the height of the electrode, the higher the efficiency of the device in terms of absorbing the optical power. Due to the errors present while growing the sample in lab, it was decided to present the final design with a range of

		Height of Electrodes (nm)										
		70	75	80	85	90	95	100	100	110	115	120
Width of Electrodes (nm)	80	0.68	0.68	0.67	0.66	0.65	0.63	0.62	0.60	0.58	0.56	0.55
	90	0.74	0.75	0.75	0.73	0.71	0.68	0.66	0.63	0.60	0.57	0.55
	100	0.82	0.82	0.81	0.79	0.75	0.71	0.68	0.64	0.60	0.57	0.54
	110	0.89	0.88	0.86	0.82	0.77	0.72	0.67	0.63	0.59	0.55	0.52
	120	0.95	0.93	0.88	0.83	0.77	0.71	0.65	0.61	0.56	0.52	0.49

Table 2.2: Fraction of optical power absorbed in the electrodes and GaAs

possible values for each parameter. As a result, upon completion of the optimization process, the following ranges were selected for each parameter:

Parameter	Minimum value (nm)	Maximum value (nm)
Width of electrodes	100	120
Height of electrodes	70	85
Si_3N_4 thickness	350	400
Top $Al_{0.32}Ga_{0.68}As$ layer thickness	260	280
GaAs thickness	190	210

Table 2.3: Acceptable range of values for different parameters

Based on the data presented in table (2.3), the wafer was decided to be grown with 200 nm of GaAs on the top as the active layer, 270 nm of $Al_{0.32}Ga_{0.68}As$ underneath the active layer, and a DBR composed of 25 periods of $Al_{0.32}Ga_{0.68}As$ and AlAs with thicknesses equal to 57 nm and 65 nm, respectively. In addition, the height and thickness of the gratings were decided to be 80 nm and 100 nm, respectively, and 370 nm of Si_3N_4 was taken to act as the anti-reflection coating. A schematic of the design is shown in figure (2.1).

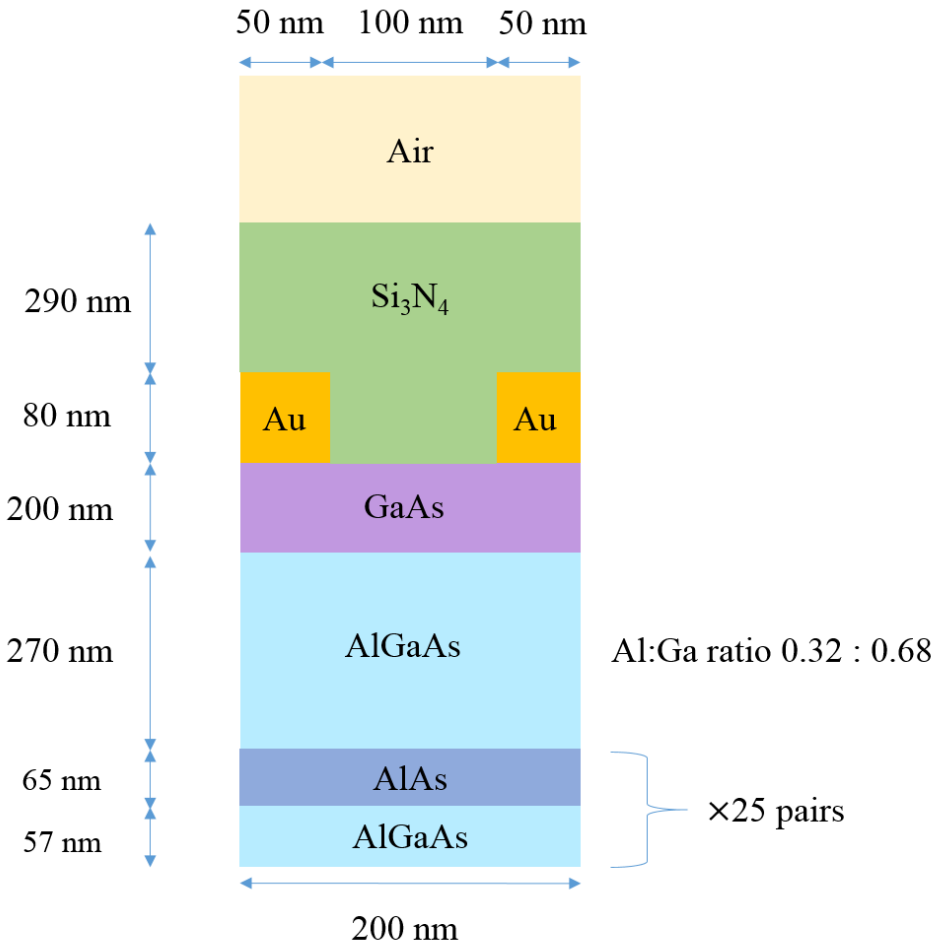

Figure 2.1: Final design

Figure 2.2 demonstrates the electric field profile with parameter values just mentioned. It is clear from the figure that the standing wave in the anti-reflection layer is relatively small in amplitude, meaning that most of the power is either absorbed by GaAs, or dissipated in the gold electrodes. Furthermore, it can also be observed that the combination of the DBR on the bottom and the electrodes on top has created a resonant cavity at the frequency of operation of the device since no power escapes from the bottom and very little power reflects away from the top.

The right plot in figure 2.2 illustrates how the intensity of the electric field increases sig-

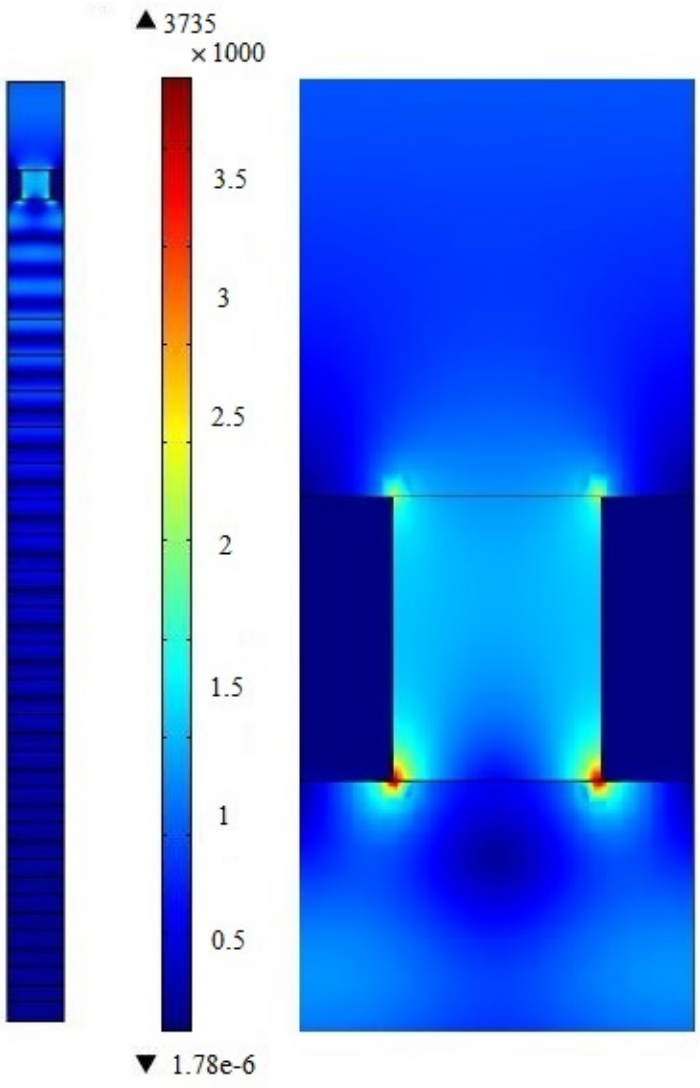

Figure 2.2: Electric field profile ($\frac{\mathrm{V}}{\mathrm{m}}$)

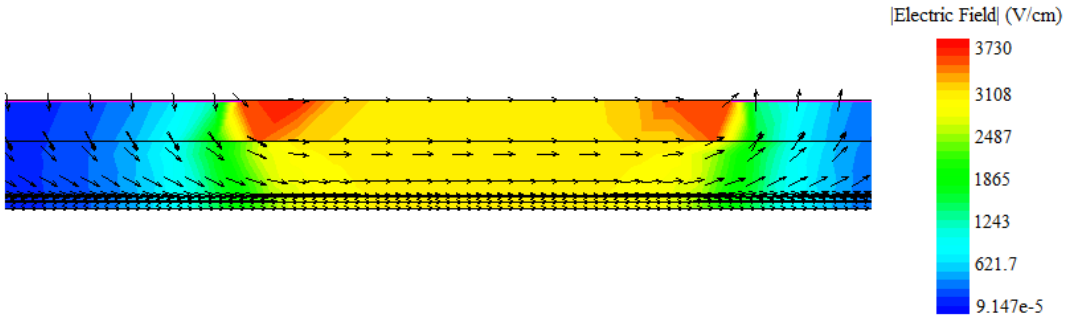

Figure 2.3: Static electric field profile

nificantly near the edges of the electrodes due to the edge effect. This is really beneficial to the operation of the device since it results in a large number of carriers being generated near the edges as opposed to other parts of the active layer.

With the optical optimization of the design finished, we can now move on to the electrical aspects of the design. As mentioned before, the final thickness of the GaAs layer should not be any higher than 200 nm. Figure 2.3 demonstrates the static electric field profile of the device when applying a 1 V voltage across the anode and cathode. It is important to mention that the simulation shown in figure 2.3 is based on the dimensions specified in figure 2.4. To be clear, the thickness of the electrodes is neglected in the Sentaurus simulations since we are only looking at the static electric field. However, the most important dimensions are the 5 μm length of gratings, the 3 μm distance between the tip of the gratings and the anode, and the 3 μm length of bias lines.

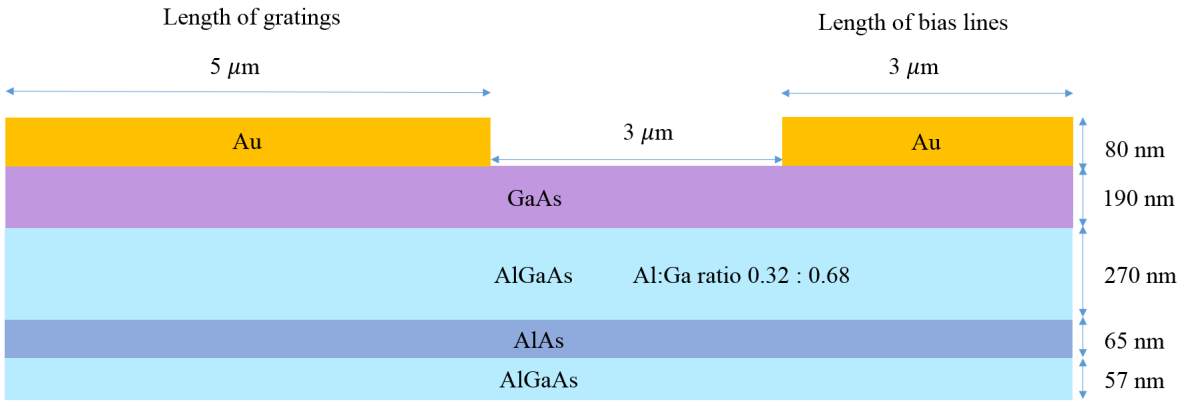

Figure 2.4: Static electric field profile

Please note that to run the electric field simulations it was necessary to simplify the design to a two-dimensional structure. Therefore, since the distance between the grated electrodes is negligible compared to the distance between the cathode and anode, and to the total width of the cathode and anode, both the cathode and anode were approximated with a uniform conductive plane. In addition, only the first couple of Bragg mirror layers are included in this figure. The reason is that as our simulations showed, the rest of the layers do not affect the electrical properties at the surface of GaAs. Optimization of the total length of the cavity (GaAs and the top DBR layer) and dimensions of the gratings was done in collaboration with my colleague, Dr. Semih Cakmakyapan. Exploring and optimizing the electrical properties of the device was done in collaboration with Sabareesh Nikhil Chinta.

Putting everything together, in the range $\lambda \in$[720 nm, 820 nm], we expect to get the results shown in figures 2.5 and 2.6 for the optical operation of the device.

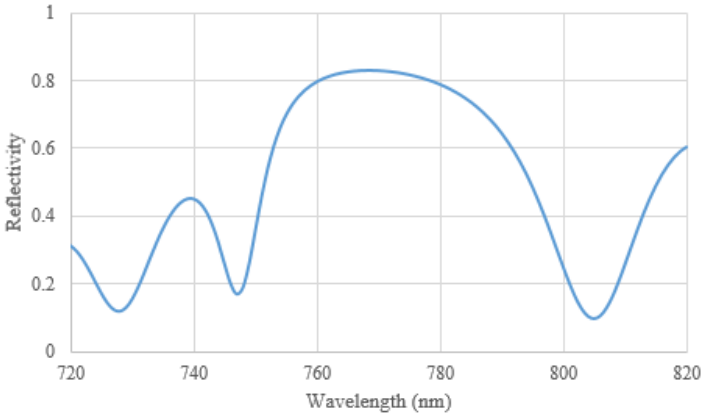

Figure 2.5: Reflectivity of the design excluding gratings (just the wafer)

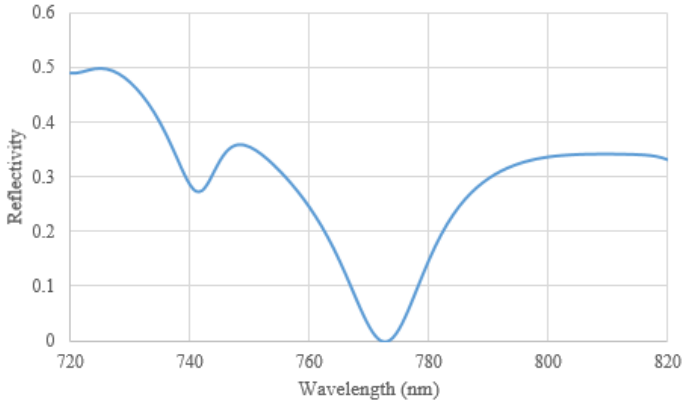

Figure 2.6: Reflectivity of the design including gratings and the anti-reflection coating

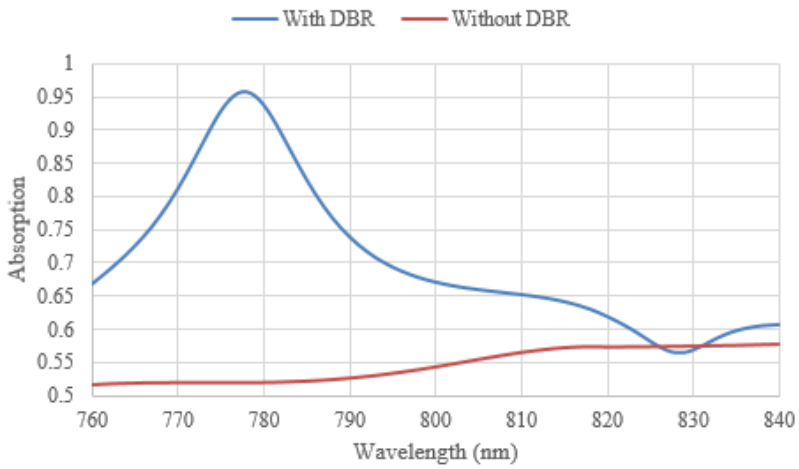

Figure 2.7: Percentage of incident power absorbed by the electrodes and GaAs

Figure 2.7 clearly illustrates the effect of the DBR in the absorption of the incident optical power by the electrodes and the GaAs layer. It is clear that by not including the distributed Bragg reflector, the absorption is below 0.6 in the 760-840 nm range, whereas, there is a clear peak at a wavelength of 778 nm with an absorption of about 96% when the DBR is incorporated into the design. Note that here we define absorption as the percentage of the optical power absorbed within the electrodes and the active layer.

Figure 2.8 represents the final fabricated and packaged device. Notice how the optical pump radiation is polarized perpendicular to the length of the gratings. This is due to the fact that coupling of electromagnetic radiation and surface plasmons is maximized when the polarization of the electric field is in a direction perpendicular to the length of the gratings. Also, THz emission occurs due to the presence of Hertzian dipole nano-antenna arrays. This leads to improved bandwidth in the device [28]. Also, due to the number of gratings present, it is clear that carrier screening is low or happens at higher incident optical powers than a conventional THz source since the carriers are generated and absorbed over a much larger area. Furthermore, due to the extendability of the device, diffraction limit has been overcome since for any beam size, it is possible to increase the area covered by gratings as need be.

An important point to notice from figure 2.8 is that the direction of photo-current in every second area between the bias lines, where no grating is present, is opposite of the direction of current in the areas covered by the plasmonic gratings. As a result, this current would lead to THz radiation which destructively interferes with the THz radiation generated by the gratings. Therefore, as will be explained in the next chapter, GaAs will be etched in every second region between the anode and cathode to eliminate the undesired THz radiation. Finally, one would expect the reflectivity of the device to be higher (or absorption to be lower) than that shown in figure 2.6 because bias lines and the etched GaAs region were not taken into account in the simulations producing that figure. This expectation will be taken into account in chapter 4, where the results of reflection measurements are presented.

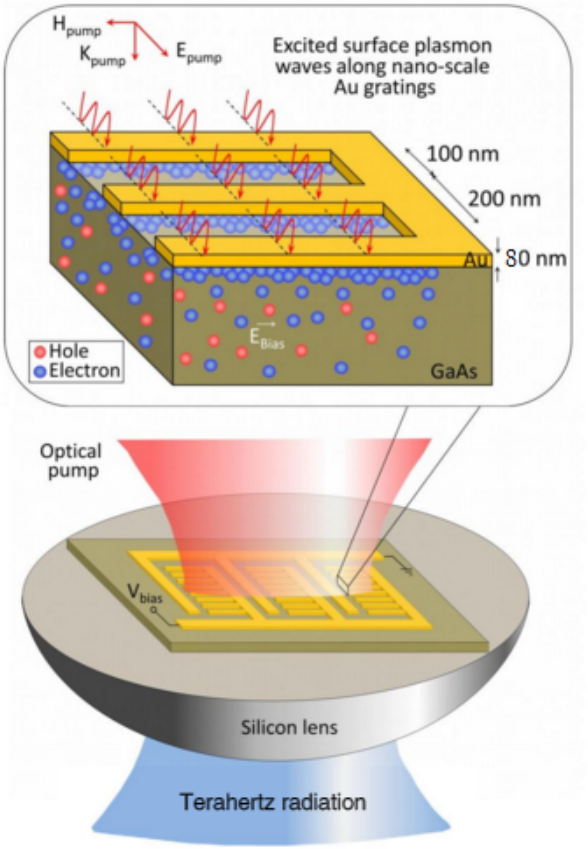

Figure 2.8: Schematic of the packaged device

Chapter 3

Procedure and Tests

In this chapter, we describe the experimental procedure and the steps taken to explore the accuracy of fabrications.

3.1 Wafer Growth

The wafer was grown on an epi-ready two inch, 001 semi-insulating GaAS (Si-GaAs) wafer. The growth was done using Molecular Beam Epitaxy (MBE) in a VEECO 930, high vacuum machine. After placement of the substrate into the load-lock chamber, it was heated to 200^{o}C and kept at that temperature for ten hours to reduce the amount of impurities, oxide layer, and water on the substrate. Subsequently, the substrate was moved into the buffer chamber, where it was heated and kept at 300^{o}C for 25 minutes to further remove impurities from the device. The wafer was then moved into the growth chamber where a high enough influx of As was continuously applied to prevent evaporation of As from the surface of the wafer. This As flow was applied throughout the growth, until the device was

cooled down to a temperature below 300^{o}C. After entering the growth chamber, the substrate temperature was raised to 578^{o}C (pyrometer reading) and quickly raised to 595^{o}C and annealed at this temperature for 10 minutes to ensure all impurities and oxide layers were removed. The crystalline quality of the surface was then explored using a high voltage RHEED machine (in-situ monitoring). 4×2 lines were clearly visible at this point. Upon completion of the deoxidization process, the substrate temperature was dropped to 585^{o}C (pyrometer reading) at which point the growth of a 200 nm buffer GaAs layer was begun to ensure surface homogeneity for the growth of the design. The growth rate of GaAS was set to 0.86 monolayers/s. To suitably grow the super-lattice structure of the DBR, the temperature of the substrate was further dropped to 565^{o}C (pyrometer reading) and kept there for about five hours and 30 minutes while the 25-period AlAs/$Al_{0.32}Ga_{0.68}As$ DBR was grown. The growth rates of AlAs and $Al_{0.32}Ga_{0.68}As$ were set to 0.4 monolayers/s and 1.26 monolayers/s, respectively. Throughout the growth of the buffer layer and DBR structure, RHEED measurements were performed to ensure high growth quality, which was verified by the existence of clear 4×2 patterns. Once the growth of the final DBR layer was finished, the temperature of the substrate was raised back to 585^{o}C (pyrometer reading), ideal for the growth of the 270 nm AlGaAs layer and the active GaAs layer on top. The crystalline quality of these layers was also rigorously monitored during growth. The rotation rate of the wafer throughout growth, which took about eight hours in total, was between 5 and 7 rpm.

Once the 200 nm active GaAs layer was grown, the temperature of the substrate was programmed to gradually drop to 300^oC, low enough to transfer the wafer into the buffer chamber. It is worth mentioning that the As influx was finally stopped when the temperature of the substrate was reduced below 300^oC. Upon extraction, the surface of the wafer was examined. The surface was completely uniform with no irregularities or color changes and had a perfect metallic mirror-like shine.

3.2 XRD Measurements

The crystalline structure and composition of the wafer were determined using double-axis HR-XRD with CuKα1 radiation in a Bede D1 diffractometer equipped with a Maxflux focusing graded X-ray mirror and a two bounce Si 220 channel-cut collimator crystal. Typical step sizes were 0.005^o for the longitudinal $2\theta - \omega$ scans, and between 0.008^o and 0.025^o for the transverse ω (rocking curve) scans. Upon the completion of scans, Bede RADS software was used to find the best-fitting composition/thickness combination to the acquired data. Figures 3.1 and 3.2 demonstrate the level of agreement between the simulations and rocking curves of the GaAs 002 and 004 peaks.

Figure 3.3 illustrates the final design using the parameters found in the XRD measurements.

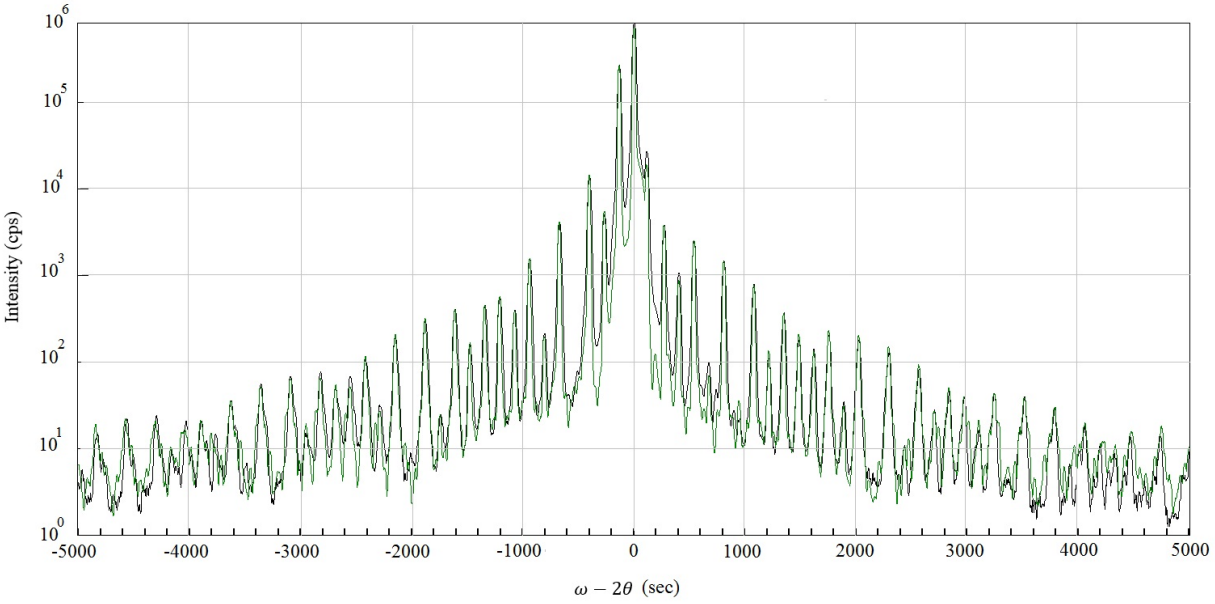

Figure 3.1: Comparison of simulations and 002 peak of GaAs rocking scan

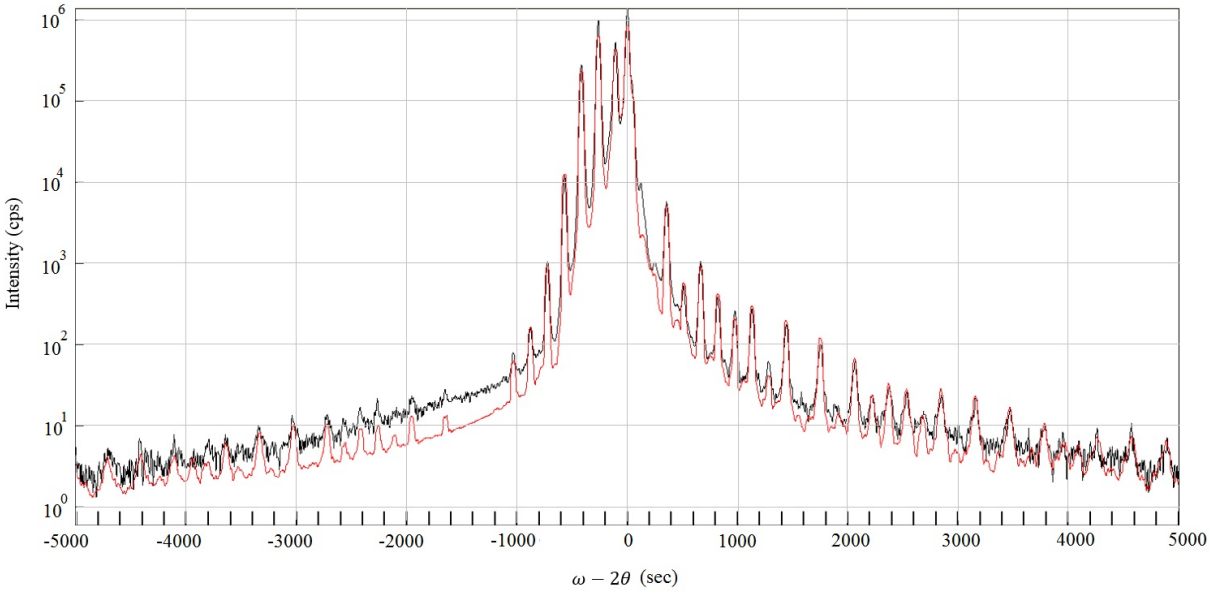

Figure 3.2: Comparison of simulations and 004 peak of GaAs rocking scan

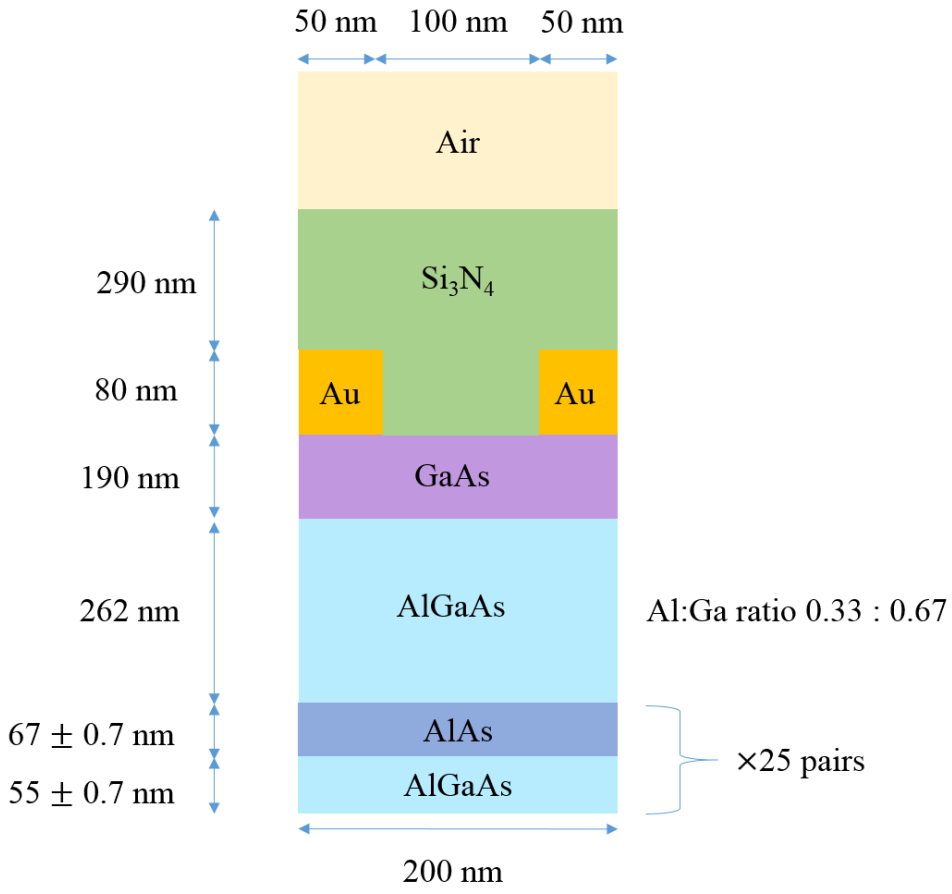

Figure 3.3: Final device

3.3 Fabricating the Gratings, Bias Lines, and Packaging

Once the XRD measurements confirmed a good agreement between the design specifications (figure 3.3) and wafer parameters, the sample was prepared for the fabrication of gratings. Initially, a standard cleaning procedure using acetone, isopropanol and DI water was performed and the sample was spin-coated with the positive tone electron beam resist PMMA (Poly-methyl methacrylate). Then, electron beam lithography was used to pattern the gratings on the resist. The sample was then developed with 1:3 MIBK:IPA for 60 sec-

onds. The developed area was then rid of residue resist by cleaning using oxygen plasma and 80 W RF power. Later, the sample was cleaned with DI:HCl 4:1 solution for 20 seconds to remove the natural oxide layer. The cleaning process was completed with rinsing the sample with DI water, which was followed by the deposition of a 2 nm titanium adhesive layer and an 80 nm gold layer using electron beam evaporation. Finally, the standard lift off process was carried out with acetone. The deposition of gratings was done by Dr. Semih Cakmakyapan.

After grating deposition, we used optical lithography to pattern the bias lines and contact pads. Then, we deposited 50 nm Ti/ 550 nm Au lines with 2 um width and contact pads using an evaporator. Subsequently, the GaAs layer on top was etched for every second gap between the anode and cathode by using an ICP RIE tool. After that, a 370 nm Si_3N_4 anti-reflection coating was deposited using a PECVD tool. Finally, the contact pads were opened using the ICP RIE tool to etch the anti-reflection coating and enable biasing of the device during operation.

The device was finally packaged on top of a 12 mm, in diameter, hemispherical Si lens in order to couple the emitted THz radiation more efficiently into the air and to collimate the beam. The fabrication of the bias lines was done by my colleague, Nezih Tolga Yardimci.

Chapter 4

Results

In this section, we present two sets of reflection measurements proving the effectiveness of the DBR. We will also include a complementary set of data illustrating the photocurrent of the device.

4.1 Reflectivity Tests

Two sets of reflection measurements were done on the device. One set of measurements was done on the device prior to the fabrication of the gratings and bias lines on top. Another set of measurements was done after the final device was packaged. Figure 4.1 illustrates the setup used to perform the reflection measurements. For these measurements, we used a tunable Ti:sapphire laser in CW (continuous wave) mode. First, we checked the power reflected from a mirror in place of the device. This power reading would be used as our reference power. Then, we placed the sample in place of the mirror and measured the reflected power from the sample for each wavelength to produce the experimental results

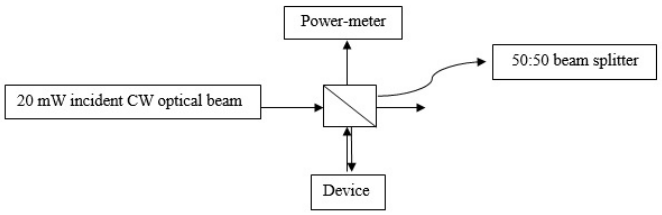

Figure 4.1: The optical setup used for reflection measurements

shown in figures 4.2 and 4.4. Finally, we divided the measured power values by the reference power levels at each wavelength to normalize the data.

It should be noted that the devices used in the optical setup were a Coherent LabMaxTo Powermeter, a BS011 - 50:50 Non-Polarizing Beam-Splitter Cube, and a tunable Ti:Sapphire laser capable of producing electromagnetic radiation with wavelength in the range [700 nm, 840 nm].

Reflectivity measurements

Figure 4.2 compares the experimental reflectivity measurements and those expected by simulations. Please note that the simulations are based on the XRD data. It is clear from the diagram that the experimental data seems to be slightly blue-shifted from the simulation results. Indeed, when the simulation results are shifted left by 10nm, the two sets of data match very well in the range 762-796 nm. This slight shift is, in part, due to the error existing in the true thickness of the DBR layers, as shown in figure 3.3, because the position of the global minimum is highly sensitive to the true thicknesses of the DBR layers. Also, as simulations showed during development of the design, the global minimum shifted by as much as 6 nm when the thickness of the active GaAs layer was changed in

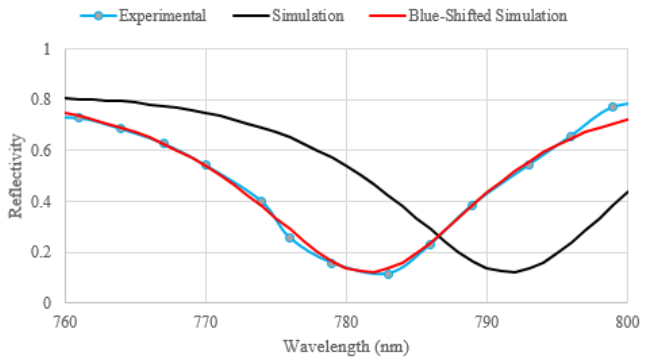

Figure 4.2: Comparison of reflectivities (no grating)

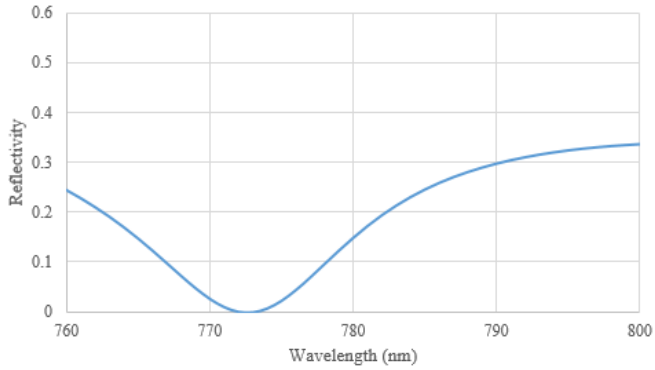

Figure 4.3: Expected reflectivity simulation result, assuming the surface of GaAs is solely covered by plasmonic gratings and anti-reflection coating (neglecting the effect of the bias lines)

steps as low as 5 nm. The XRD measurements, however, were not as sensitive to the thickness of the top GaAs layer. Furthermore, although reliable sources were used to predict the reflection coefficients of the materials, slight differences between these coefficients in the design and the device could easily shift the plot. The main source of error, however, is not having enough data points and the drift of the center laser frequency during the experiments. Keeping the optical pump power constant throughout measurements was also really difficult, and this could have added to the discrepancies observed. Putting all these together, a global minimum shift of 10 nm is completely tolerable.

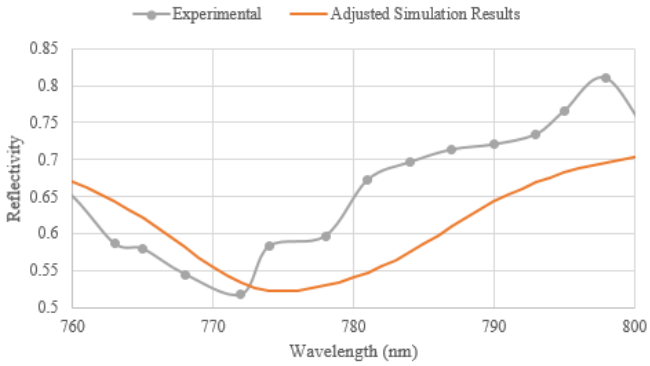

Figure 4.4: Comparison of reflectivities using equation (4.1)

Figure 4.4 compares the adjusted simulation results with the experimental results for reflectivity in the final device. The adjustment of the simulations is based on the areas covered by the gratings, GaAs, and bias lines. Looking at figure 2.8 again, it can be observed that the whole structure has a period of repetition. The thickness of the bias lines is 2 μm, the length of the gratings is 5 μm, the distance between the tip of the gratings and the anode is 3 μm, and the distance between every second anode and cathode is 3 μm. In addition, it is clear that every period consists of two bias lines, one full length of gratings, one gap area between the gratings and the anode, and one gap area between the anode and cathode, which, as previously mentioned, has its GaAs layer etched. As a result, the period length is 15 μm. Thus, the reflectivity of the device at each wavelength can roughly be found from the following formula:

$$R \approx \frac{5}{15}R(\text{gratings}) + \frac{2\times 2}{15}R(\text{bias lines}) + \frac{3}{15}R(\text{wafer}) + \frac{3}{15}R(\text{wafer without GaAs})$$

Assuming that R(bias lines) = 1, R(wafer without GaAs) = 1 because of the existence of the DBR and no absorption, R(wafer) is as given in figure 4.2 (blue curve), and R(gratings) follows the diagram given in figure 4.3, we arrive at equation (4.1)

$$R \approx \frac{7}{15} + \frac{1}{3}R(\text{gratings}) + \frac{1}{5}R(\text{wafer}) \tag{4.1}$$

Figure 4.4 shows the comparison between the adjusted simulation results, based on equation (4.1), and the experimental results. Other than the general trend and the rough position of the global minimum in the graph, the two plots do not look similar at all. Despite its poor estimation of the gathered data, equation (4.1) gives us an idea on how to determine if our experimental data could follow the simulated results or not. Let us generalize equation (4.1) to the following:

$$R \approx \frac{15-a}{15} + \frac{b}{15}R(\text{gratings}) + \frac{a-b}{15}R(\text{wafer}) \tag{4.2}$$

where $15 - a$ represents the effective combined length of the bias lines and the etched gas region, b represents the effective length of the gratings, and $a - b$ represents the effective length of the region between the tip of the gratings and the anode.

By finding the best fit from equation (4.2) and the experimental data, we get the result shown in figure 4.5, where $a = 8.8$ and $b = 3.4$.

In figure 4.5, the blue curve represents the direct result of equation (4.2) and the orange curve is the same curve blue-shifted by 6 nm. Again, a 6 nm shift is within the range of error we could have for our device, since, similar to figure 4.2, the error in the dimensions of the gratings after fabrication could have moved the global minimum slightly.

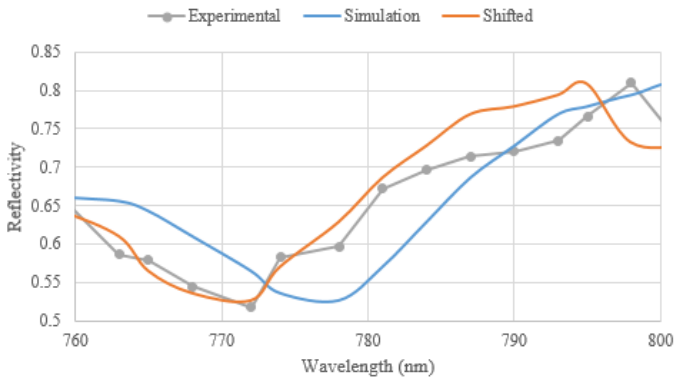

Figure 4.5: Comparison of reflectivities using equation (4.2), $a = 8.8$, and $b = 3.4$

It is important to note that, to produce figure 4.4, the blue-shifted simulation results from figure 4.2 (red plot) were used to represent R(wafer), whereas in figure 4.4, the experimental results from figure 4.2 (blue plot) were used to represent R(wafer).

The author gratefully acknowledges Dr. Semih Cakmakyapan and Nezih Tolga Yardimci for performing the reflectivity measurements.

4.2 Current Measurements

To further illustrate the effectiveness of the distributed Bragg reflector in increasing the photocurrent, and consequently, the THz power generated, we allocate this section to view the results of photo-current measurements on the device.

Figure 4.6 illustrates the total current under a 10 mW optical pump power and 10 V bias voltage.

It is perfectly clear from figure 4.6 that the current profile roughly follows the absorption spectrum we would expect, given the reflectivity profile in figure 4.5, and the expected absorption we observed in figure 2.7. In addition, the maximum current happens at an opti-

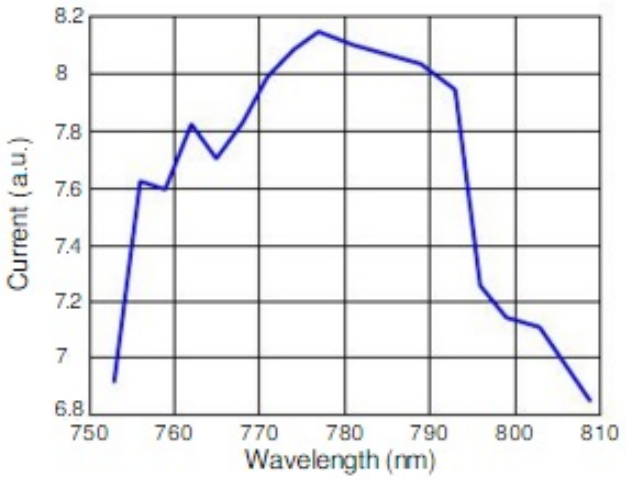

Figure 4.6: Measured current when $V_{bias} = 10$ V and $P_{incident} = 10$ mW

cal wavelength around 776 nm, which is very close to the global minimum reflectivity we found in figure 4.5. The error may be attributed to not having enough data points, the difficulty in maintaining a constant power level throughout the experiments, and the amount of drift in the central frequency of the Ti:Sapphire laser.

It should also be mentioned that although the current profile reflects the effects of the DBR, the overall shape of the plot does not completely match what we would expect given figure 4.5. The main reason is that one may not assume that all the power that got transmitted into the device was completely absorbed by the GaAs layer, because some of the power transmitted could have escaped from the bottom of the DBR. This is because the DBR is completely reflective only at certain wavelengths and not all.

Chapter 5

Conclusions

In summary, we demonstrated the design of a photoconductive THz source incorporating a distributed Bragg reflector that, when combined with a suitable plasmonic grating design on the active layer, is capable of theoretically trapping all of the incident optical pump power within itself. After growth and fabrication of the device, the results of reflectivity measurements performed both on the final device and on the device prior to the fabrication of plasmonic gratings, and a preliminary set of current measurements were presented and compared to theoretical expectations. These comparisons clearly illustrated the effects of the DBR in producing an optical cavity capable of trapping most of the incident optical power. Given the level of agreement between the design and the final device, it is clear that developing next-generation plasmonic terahertz sources could be enhanced greatly by incorporating distributed Bragg reflectors.

Bibliography

[1] Tonouchi, M. Cutting-edge terahertz technology. *Nat. Photonics* **1**, 97-105 (2007).

[2] Eisele, H. & Haddad, G. Two terminal millimeter-wave sources. *IEEE Trans. Microwave Theory Tech.* **46**, 739–746 (1998).

[3] Maestrini, A., Ward, J., Gill, J., Javadi, H., Schlecht, E., Chattopadhyay, G., Maiwald, F., Erickson, N. R. & Mehdi, I. A 1.7-1.9 THz local oscillator source. *IEEE Microwave Wireless Component Lett.* **14**, 253–255 (2004).

[4] Momeni, O. & Afshari, E. High power terahertz and sub-millimeter-wave oscillator design: a systematic approach. *IEEE J. Solid-State Circuits* **46**, 583–597 (2011).

[5] Maestrini, A., Ward, J., Gill, J., Lee, C., Thomas, B., Lin, R., Chattopadhyay, G. & Mehdi, I. A Frequency-Multiplied Source With More Than 1 mW of Power Across the 840–900-GHz Band. *Microwave Theory and Techniques, IEEE Transactions* **58**, 1925-1932 (2010).

[6] Mehdi, I., Ward, J., Maestrini, A., Chattopadhyay, G., Schlecht, E., Thomas, B., Lin, R., Lee, C. & Gill, J. Broadband sources in the 1–3 THz range. *Proc. 34th Int. Infrared, Millimeter, Terahertz Waves Conf.* 1-2 (2009).

[7] Gold, S. H. & Nusinovich, G. S. Review of high-power microwave source research. *Rev. Sci. Instrum.* **68**, 3945–3974 (1997).

[8] Tucek, J., Kreischer, K., Gallagher, D., Vogel, R. & Mihailovich, R. A compact, high power, 0.65 THz source. *Proc. 9th Int. Vacuum Electron. Conf.* 16–17 (2008).

[9] Gorshunov, B. P., Volkov, A. A., Prokhorov, A. S. & Spektor, I. E. Methods of terahertz-sub-terahertz BWO spectroscopy of conducting materials. *Phys. Solid State* **50**, 2001–2012 (2008).

[10] Scalari, G., Walther, C., Fischer, M., Terazzi, R., Beere, H., Ritchie, D. & Faist J. THz and sub-THz quantum cascade lasers. *Laser Photon. Rev.* **3**, 45–66 (2009).

[11] Sasaki, Y., Avetisyan, Y., Kawase, K. & Ito, H. Terahertz-wave surface-emitted difference frequency generation in slant-stripe-type periodically poled LiNbO3 crystal. *Appl. Phys. Lett.* **81**, 3323–3325 (2002).

[12] Vodopyanov, K. L., Fejer, M. M., Yu, X., Harris, J. S., Lee, Y.-S., Hurlbut, W. C., Kozlov, V. G., Bliss, D. & Lynch, C. Terahertz wave generation in quasi-phase-matched GaAs. *Appl. Phys. Lett.* **89**, 141119 (2006).

[13] Stepanov, A., Kuh, J., Kozma, I., Riedle, E., Alma'si, G. & Hebling, J. Scaling up the energy of THz pulses created by optical rectification. *Opt. Express* **13**, 5762–5768 (2005).

[14] Berry, C. W., Hashemi, M. R., Unlu, M. & Jarrahi, M. Significant performance enhancement in photoconductive terahertz optoelectronics by incorporating plasmonic contact electrodes. *Nat. Commun.* 4:1622 doi: 10.1038/ncomms2638 (2013).

[15] Shi, W., Ding, Y. J., Fernelius, N. & Vodopyanov, K. Efficient, tunable, and coherent 0.18–5.27-THz source based on GaSe crystal. *Opt. Lett.* **27**, 1454–1456 (2002).

[16] Preu, S., Dohler, G. H., Malzer, S., Wang, L. J. & Gossard, A. C. Tunable, continuous-wave terahertz photomixer sources and applications. *J. Appl. Phys.* **109**, 061301 (2011).

[17] Bjarnason, J. E., Chan, T. L. J., Lee, A. W. M., Brown, E. R., Driscoll, D. C., Hanson, M., Gossard, A. C. & Muller, R. E. ErAs:GaAs photomixer with two-decade tunability and 12μW peak output power. *Appl. Phys. Lett.* **85**, 3983–3985 (2004).

[18] Peytavit, E., Lepilliet, S., Hindle, F., Coinon, C., Akalin, T., Ducournau, G., Mouret, G. & Lampin, J.-F. Milliwatt-level output power in the sub-terahertz range generated by photomixing in a GaAs photoconductor. *Appl. Phys. Lett.* **99**, 223508 (2011).

[19] Upadhya, P. C., Fan, W., Burnett, A., Cunningham, J., Davies, A. G., Linfield, E. H., Lloyd-Hughes, J., Castro-Camus, E., Johnston, M. B. & Beere, H. Excitation-density-dependent generation of broadband terahertz radiation in an asymmetrically excited photoconductive antenna. *Opt. Lett.* **32**, 2297–2299 (2007).

[20] Roehle, H., Dietz, R. J. B., Hensel, H. J., Böttcher, J., Künzel, H., Stanze, D., Schell, M. & Sartorius, B. Next generation 1.5 mm terahertz antennas: mesa-structuring of InGaAs/InAlAs photoconductive layers. *Opt. Express* **18**, 2296–2301 (2010).

[21] Taylor, Z. D., Brown, E. R. & Bjarnason, J. E. Resonant-optical-cavity photoconductive switch with 0.5% conversion efficiency and 1.0W peak power. *Opt. Lett.* **31**, 1729–1731 (2006).

[22] Park, S. -G., Jin, K. H., Yi, M., Ye, J. C., Ahn, J. & Jeong, K. -H. Enhancement of terahertz pulse emission by optical nanoantenna. *ACS NANO* **6**, 2026–2031 (2012).

[23] Auston, D. H., Cheung, K. P. & Smith, P. R. Picosecond photocoducting Hertzian dipoles. *Appl. Phys. Lett.* **45**, 284–286 (1984).

[24] Berry, C. W. & Jarrahi, M. Terahertz generation using plasmonic photoconductive gratings. *New J. Phys.* **14**(10), 105029 (2012).

[25] Preu, S., Dohler, G. H., Malzer, S., Wang, L. J. & Gossard, A. C. Tunable, continuous-wave terahertz photomixer sources and applications. *J. Appl. Phys.* **109**, 061301 (2011).

[26] Jackson, A. W., Ibbetson, J. P., Gossard, A. C. & Mishra, U. K. Reduced thermal conductivity in lowtemperature grown GaAs. *Appl. Phys. Lett.* **74**, 2325–7 (1999).

[27] Yang, S. H., Hashemi, M. R., Berry, C. W. & Jarrahi, M. 7.5% optical-to-terahertz conversion efficiency offered by photoconductive emitters with three-dimensional plasmonic contact electrodes. *IEEE Trans. Terahertz Sci. Technol.* **4**(9), pp. 575–581 (2014).

[28] Yardimci, N. T., Yang, S.-H., Berry, C. W. & Jarrahi, M. Terahertz Radiation Enhancement in Large-Area Photoconductive Sources by Using Plasmonic Nanoantennas. *Proc. Conference of Lasers and Electro-Optics* (2015).

[29] Polyanskiy, M. N. Refractive index database. Available at http://refractiveindex.info (accessed Nov. 20 2015).

[30] Sheppard, C. J. R. Approximate calculation of the reflection coefficient from a stratified medium. *Pure Appl. Opt.* **4**, 665 (1995).